



Research Paper

Enhanced photocatalytic hydrogen evolution performance of mesoporous graphitic carbon nitride co-doped with potassium and iodine



Yarong Guo, Qiong Liu, Zehao Li, Zhengguo Zhang, Xiaoming Fang*

Key Laboratory of Enhanced Heat Transfer and Energy Conservation, The Ministry of Education, School of Chemistry and Chemical Engineering, South China University of Technology, Guangzhou 510640, China

ARTICLE INFO

Keywords:

Photocatalysis
Graphitic carbon nitride
Co-doping
Mesoporous structure
Hydrogen evolution rate

ABSTRACT

The potassium and iodine co-doping combined with a mesoporous structure for developing a novel g-C₃N₄-based photocatalyst is constructed. The K and I co-doped mesoporous g-C₃N₄ has been successfully synthesized via the one pot thermal polymerization of a mixture consisting of dicyandiamide, KI, and SBA-15 used as the hard template. It is shown that this photocatalyst consists of short rod-like network with plenty of pores openings into their surfaces. The mesoporous structure and the doping with K and I in it have been verified by several techniques. For this photocatalyst, a blue shift of the optical absorption band edge induced by the mesoporous structure is compensated for by the red shift originated from the co-doping with K and I. This photocatalyst exhibits the longest life time of carries, the fastest charge transport, and the highest photocurrent density as compared with the mesoporous g-C₃N₄ and the K and I co-doped one. It is revealed a synergistic effect between the formation of the mesoporous structure and the co-doping with K and I. The synergistic effect make the K and I co-doped mesoporous g-C₃N₄ photocatalyst achieves a high hydrogen evolution rate of 80.58 μmol/h, 9.7 times as high as that for pristine g-C₃N₄. These results may shed light on the integration of different modification strategies for developing novel g-C₃N₄-based photocatalysts with much enhanced photocatalytic activity.

1. Introduction

Hydrogen is a green energy since water is its only combustion product. Among all the ways for producing hydrogen, photocatalytic water splitting using solar energy has been considered as the most ideal one [1,2]. Developing robust photocatalysts with high efficiency, good stability and low cost is essential to put this hydrogen generation technology into practical applications [3–5]. Graphitic carbon nitride (g-C₃N₄), a polymer semiconductor consisting of conjugated graphitic planes composed of abundant nitrogen-containing tri-s-triazine repeating moieties, has been exemplified as a promising photocatalyst for hydrogen evolution, owing to its advantages of visible light response, wide material source and good chemical stability [6]. However, the photocatalytic activity of g-C₃N₄ is not high enough for practical applications due to some drawbacks inherent in it [7,8]. First, the band gap of g-C₃N₄ is relatively large, making it only absorb the light with wavelengths less than 450 nm [9]. Second, the intrinsic organic π -conjugated polymer structure results in fast charge carrier recombination in g-C₃N₄ [10]. Third, although the theoretical specific area of g-C₃N₄ is large, the stacking of the polymeric layers endows it with low specific area [11]. Apparently, it is highly necessary to overcome these

shortcomings of g-C₃N₄, with the purpose of developing novel g-C₃N₄-based photocatalysts with high photocatalytic activity.

Recently, various strategies have been explored to modify g-C₃N₄ for improving its photocatalytic activity [12–16], which mainly include combining with other semiconductors to construct composite photocatalysts [17–20], doping with elements or molecules to modulate the electronic structure of g-C₃N₄ [21–24], and changing its morphology from bulk to nanostructures such as nanorods, nanofibers, nanospheres, nanocapsules and nanosheets [25–30]. Combination with other semiconductors is an effective way to enhance the photocatalytic performance of g-C₃N₄ through forming the heterojunctions or Z-scheme systems [31–35]. But challenges remain in precisely controlling the microstructures of the composite photocatalysts, due to their two or more than two different components. It has been shown that, however, changing the morphology of g-C₃N₄, especially from bulk to mesoporous structure, not only is conducive to providing readily access channels to shorten the diffusion lengths of charges, but also can offer more surface active sites for surface reactions [36,37]. The doped g-C₃N₄ photocatalysts, realized by inserting metal and/or non-metal ions into the framework of g-C₃N₄ [11,38], have been reported to exhibit enhanced photocatalytic activity, because the doping with metal or

* Corresponding author.

E-mail address: cexmfang@scut.edu.cn (X. Fang).

nonmetal elements usually has the functions of effectively suppressing the recombination rate of charge carriers as well as narrowing the band gap of $g\text{-C}_3\text{N}_4$ [39–43]. However, it is obvious that one of those strategies cannot overcome all of the aforementioned shortcomings of $g\text{-C}_3\text{N}_4$ simultaneously, and the incorporation of these strategies is needed. More recently, the integration of the formation of mesoporous structure with the doping with nonmetal elements including S, O or C [38,44–47], has been employed to modify $g\text{-C}_3\text{N}_4$. And a synergistic effect between the two strategies has been found, which endowed the obtained photocatalysts with remarkably improved photocatalytic activity [44,48]. Apparently, the combination between forming mesoporous structure with element doping is an effective route for further increasing the photocatalytic activity of $g\text{-C}_3\text{N}_4$.

In our previous work, the KI-doped $g\text{-C}_3\text{N}_4$ photocatalyst has been developed, which exhibited improved photocatalytic activity in hydrogen evolution. And it has been revealed that, the doping with I resulted in a red shift in optical absorption edge, and the K doping led to the decrease in carrier recombination [49]. In the current work, aiming at making a further improvement in photocatalytic activity, the KI doping was combined with the formation of ordered mesoporous structure, and thus a KI-doped mesoporous $g\text{-C}_3\text{N}_4$ photocatalyst was developed. Specifically, the potassium and iodine co-doped mesoporous $g\text{-C}_3\text{N}_4$ photocatalyst was synthesized via the thermal polymerization of a mixture containing dicyandiamide, KI, and SBA-15 that was used as a hard template. The morphology, structure, surface chemical states, and specific surface area of the KI-doped mesoporous $g\text{-C}_3\text{N}_4$ photocatalyst were characterized, and its optical absorption, photoluminescent and photoelectrochemical properties along with photocatalytic activity for hydrogen evolution were measured. It is found that the K and I co-doped mesoporous $g\text{-C}_3\text{N}_4$ photocatalyst exhibits superior photocatalytic activity over the K-I co-doped and the mesoporous ones, owing to a synergistic effect between the K and I doping with the mesoporous structure. This work might shed light on developing high-performance $g\text{-C}_3\text{N}_4$ photocatalysts through the combination of multiple modifications.

2. Experimental section

2.1. Materials

SBA-15 was purchased from Nanjing XF Nano Material Tech Co., Ltd. Other chemicals used in the experiments were purchased from Richjoint Chemical Reagents Co., Ltd. in chemical grade purity without further purification.

2.2. Preparation

K and I co-doped ordered mesoporous $g\text{-C}_3\text{N}_4$ was prepared according to Scheme 1. 1 g of SBA-15 was ultrasonically dispersed into 25 mL of deionized water for 30 min. After that, 2 g of dicyandiamide (DCDA) and 0.12 g of potassium iodine were added into the solution with continuous stirring at 80 °C to make them dissolved, followed by drying at 80 °C to remove the water. The resultant solid was calcined at 550 °C for 4 h in a muffle furnace. Finally, the obtained sample was immersed into 50 mL of the 2 M NH_4HF_2 solution with vigorous stirring for 24 h to remove the hard template. After being centrifuged and washed for several times, the K and I co-doped ordered mesoporous $g\text{-C}_3\text{N}_4$ sample was obtained and denoted as MP-CN-KI. For comparison purposes, ordered mesoporous $g\text{-C}_3\text{N}_4$ was synthesized using the same procedure without adding the potassium iodine and denoted as MP-CN. And K and I co-doped $g\text{-C}_3\text{N}_4$ was prepared by the same procedure without adding SBA-15 and denoted as CN-KI. In addition, pristine $g\text{-C}_3\text{N}_4$ was prepared by calcining DCDA at 550 °C for 4 h and denoted as CN.

2.3. Characterization

Wide and small angle powder X-ray diffraction (XRD) patterns were obtained using a Bruker D8 Advance X-ray diffractometer with $\text{Cu-K}\alpha 1$ ($\lambda = 1.5418 \text{ \AA}$) as the source. The infrared absorption spectra were gained from a Vector 33 Fourier transform infrared spectrometer (FT-IR). X-ray photoelectron spectroscopy (XPS) data were carried out on KRATOS Amicus instrument with a monochromatized $\text{Al-K}\alpha$ line source (200 W). The Brunauer-Emmett-Teller (BET) surface area and pore size distribution measurements were measured at 77 K on a Quantachrome Nova 2000e surface area analyzer. The morphologies and microstructures were observed through a Zeiss Merlin Compact fieldemission scanning electron microscope (SEM) and a JEOLJEM 2100F fieldemission electron microscope (TEM) instrument. UV-vis diffuse reflection spectra (DRS) were recorded on a U-3010 spectrophotometer. Photoluminescence (PL) spectra were obtained from an F-4500 Fluorescence Spectrophotometer at room temperature with the excitation wavelength at 375 nm. The time-resolved fluorescence spectra were obtained on FLSP920 steady/transient fluorescence spectrophotometer. The solid electron spin resonance (ESR) measurements were analyzed using a Bruker model A300 spectrometer equipped with a 300 W Xe lamp with a UV-cutoff ($> 420 \text{ nm}$) as the visible light source.

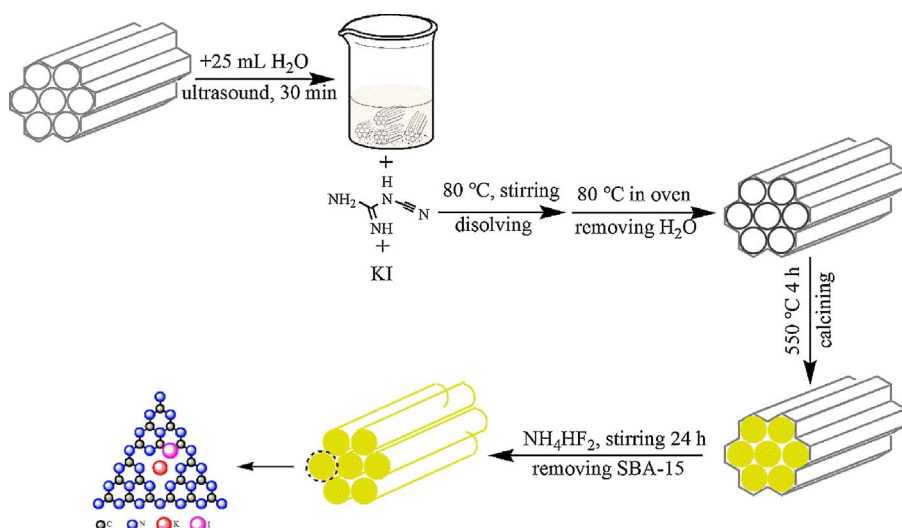
2.4. Photocatalytic activity evaluation

Photocatalytic water splitting for hydrogen evolution was carried out in an outer top-irradiation reaction vessel (250 mL) connected to a closed glass gas circulation system. Typically, 50 mg of each catalyst powder was dispersed in 100 mL methanol solution (5 vol%) where methanol served as sacrificial electron donor. Pt (1 wt%) was loaded on the surface of the catalyst as co-catalyst using H_2PtCl_6 by in-situ photodeposition method. The reaction system was vacuumized for 1 h to remove air completely before the irradiation by a 300 W Xenon lamp (PerfectLight, China, LX300F) with a 420 nm cutoff filter and the average light intensity is detected to be 210 mW/cm^2 by the irradiometer. Cold water circulation was conducted during the reaction to keep the temperature of the reaction solution maintained at 5 °C. The evolved gas was measured every hour by gas chromatography with N_2 as the carrier gas lasting for 3 h.

The stability of MP-CN-KI was tested as follows. Firstly, MP-CN-KI (1 wt% Pt) was used to catalyze the photocatalytic hydrogen evolution for the first 3 h using the method mentioned above. Then, the reaction system was vacuumized 1 h to remove the generated H_2 gas completely. After that, the photocatalytic reaction was continued for another 3 h. The whole reaction was circulated five times (15 h in total).

2.5. Photoelectrochemical analysis

The film electrodes used in photoelectrochemical measurements were fabricated as follows. 0.1 g of the photocatalyst powder and 0.01 g of ethylcellulose were mixed, followed by being grinded into fine slurries with ethanol solution. Then the slurry was coated onto fluoride-tin oxide (FTO) conductive glass sheet using the doctor-blading technique, followed by drying at 120 °C for 1 h. The photoelectrochemical analysis was performed in a conventional three-electrode cell connected to an electrochemical analyzer (CHI660E), using a Pt sheet and an Ag/AgCl electrode as the counter and reference electrodes, respectively. The electrode were immersed in a sodium sulfate electrolyte solution (0.2 M), and the exposed effective area of the working electrode was 1 cm^2 . The periodic on/off photocurrent response of each film electrode was carried out at 0.5 V bias vs. Ag/AgCl. For electrochemical impedance spectroscopy (EIS) experiments, the perturbation signal was 0.5 V with the frequency ranging from 100 kHz to 10 mHz.



Scheme 1. The process for preparing a KI doped porous g-C₃N₄ photocatalyst.

3. Results and discussion

3.1. Structure and morphology

Fig. 1 shows the wide-angle and small-angle XRD patterns of the as-prepared g-C₃N₄ samples. Two distinct peaks referring to g-C₃N₄ can be found for all the g-C₃N₄ samples (Fig. 1A). The intense (002) diffraction peak at around 27.1° represents the inter-planar graphitic stacking, while the weak one at around 13.0° stands for an inter-planar separation [22]. For all the modified g-C₃N₄ samples, a weakness in intensity for both the diffraction peaks at 27.1° and 13.0° has been found, indicating that the in-plane structure is destroyed or changed [50,51]. As

shown in Fig. 1B, a small peak at around 1.6° is observed in the XRD patterns of both MP-CN and MP-CN-KI, while it is absent in those of CN and CN-KI. This small peak is the characteristic of a mesoporous structure containing short-ranged order in the pore arrangement [52]. It can be inferred that MP-CN and MP-CN-KI do possess a short-range ordered mesoporous structure.

Similar FT-IR spectra related to the typical CN heterocycles skeletal vibration are noticed for all the g-C₃N₄ samples (Fig. 2). The two peaks located at 810 cm⁻¹ and 1200–1600 cm⁻¹ refer to the representative breathing and stretching vibration modes of the heptazine heterocyclic ring (C₆N₇), respectively, which verify the formation of a triazine phase in all the g-C₃N₄ samples [53]. Different from pristine CN, MP-CN, CN-KI and MP-CN-KI show a peak located at around 2104 cm⁻¹, which can be ascribed to the formation of azide groups [54]. It is suggested that the morphology modulating using SBA-15 or the doping with KI both can lead to the formation of azide groups, which may be derived from the Si or K doping [55]. The broad peak at 2900–3500 cm⁻¹ attributes to the N–H vibration and the O–H vibration, derived from the surface uncondensed amine groups and the absorbed water molecules [56]. Interestingly, this peak for MP-CN and MP-CN-KI is much broader and stronger than that for CN, suggesting the existence of more uncondensed amino groups on their surfaces, arisen from the typical pore structure of the mesoporous materials [57].

The compositions and chemical states of g-C₃N₄ were examined by XPS. As illustrated in Fig. 3A. The elements of C, N, and O are observed in the survey spectra of all the g-C₃N₄ samples, where O emerges from the high-temperature synthesis in air. For CN-KI and MP-CN-KI, both K

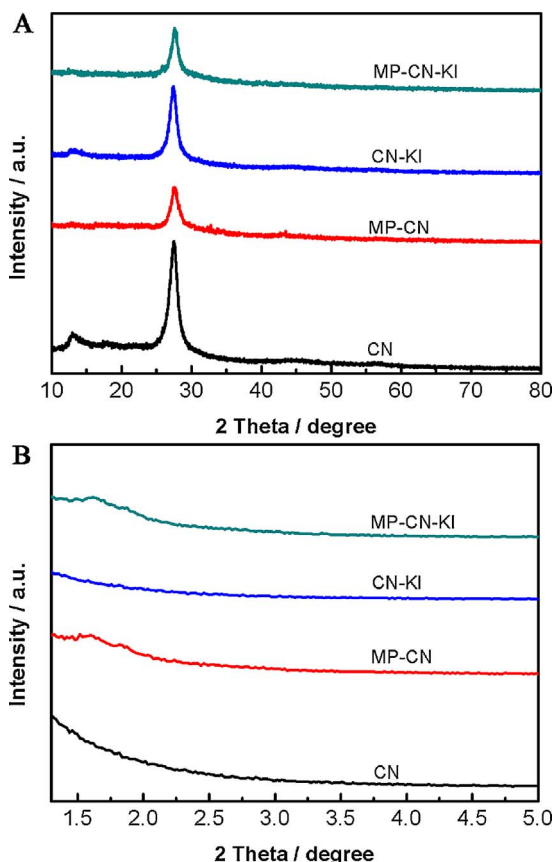


Fig. 1. Wide-angle (A) and small-angle (B) powder XRD patterns for g-C₃N₄ samples.

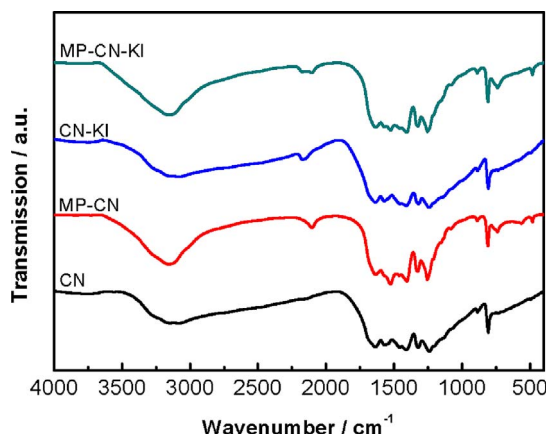


Fig. 2. FT-IR spectra of g-C₃N₄ samples.

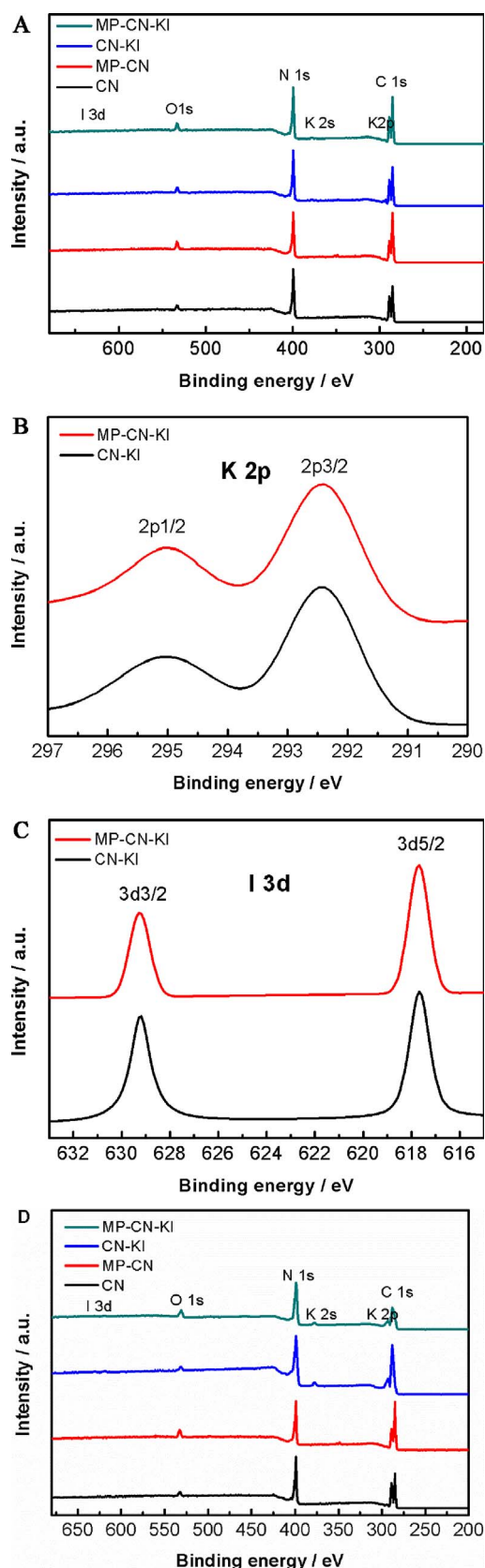


Fig. 3. XPS spectra of g-C₃N₄ samples: Survey (A), K2p (B), I3d (C) and survey after etching (D).

and I are detected (Fig. 3B and C), indicating the successful incorporation of both K and I into g-C₃N₄ network. The K2p_{3/2} and K2p_{1/2} peaks of CN-KI and MP-CN-KI are located at around 292.5 and 295.2 eV, with binding energies lower than those of potassium salts [58]. Similarly, the peaks of I3d_{3/2} and I3d_{5/2} at around 630.9 eV and 619.4 eV in CN-KI and MP-CN-KI are lower than those in iodine salts, implying the existence of the covalent bond between I and g-C₃N₄ [59]. It is also demonstrated that K and I ions doped into CN-KI and MP-CN-KI. CN-KI and MP-CN-KI exhibit almost the same peak positions, indicating that the formation of the porous structure under the aid of SBA-15 during doesn't affect the doping with K and I. As for the doping sites of K and I, according to the previous studies [40,43,49], K ions was coordinated to the big C–N rings formed by N-bridges, while I ions substituted the sp²-bonded N. In addition, the XPS measurement also has been employed on the samples after being etched with Ar for 10 nm (Fig. 3D), and the C, N, O, K and I contents in the samples before and after being etched have been obtained and listed in Table 1. No obvious decreases over the K and I contents are found after the samples etched with Ar. It is verified that K and I atoms is indeed doped into the lattice of g-C₃N₄, not just on the surface.

The N₂ adsorption–desorption isotherms and pore-size distribution curves of g-C₃N₄ samples were evaluated using the BET isotherms (Fig. 4), together with their corresponding specific surface areas (*S*_{BET}) and pore volumes (Table 2). Each sample shows a typical type IV isotherm, confirming the existence of a mesoporous structure. The hysteresis loops for MP-CN and MP-CN-KI are divided into H1 and H3 type while those for CN and CN-KI are H3, indicating that ordered cylindrical pore channels are present in MP-CN and MP-CN-KI [60]. As shown in Fig. 4B, the pore size distributions for all the samples are centered at 3–8 nm, with the pore volume increasing from 0.055 and 0.067 cm³/g for CN and CN-KI to 0.10 and 0.12 cm³/g for MP-CN and MP-CN-KI, respectively. Similarly, there is a significant increase in *S*_{BET} from 8.31 m²/g for CN to 49.09, 30.97 and 71.48 m²/g for MP-CN, CN-KI and MP-CN-KI. It is obvious that MP-CN-KI has the largest surface area and pore volume among all the samples.

SEM and TEM have been employed to detect the microstructure of the g-C₃N₄ samples. As displayed in Fig. 5, pristine CN shows a bulk structure, while CN-KI presents a looser layered structure. For the MP-CN and MP-CN-KI samples, they consist of short rod-like particles, whose morphologies are similar to that of the hard template SBA-15 [61]. And plenty of pore openings are found on the surfaces of the short rod-like particles. Furthermore, the TEM images of these g-C₃N₄ samples are displayed in Fig. 6. A thick and a thin graph-like layered structure is observed for both CN and CN-KI, similar to those previously reported results [53]. In contrast, periodic mesoporous channels with a linear array in a certain range are easily distinguished from the TEM images of MP-CN and MP-CN-KI, in accordance with the results obtained from the XRD patterns (Fig. 1B) and the BET results (Fig. 4). Compared with MP-CN, MP-CN-KI exhibits a looser structure with low ordering at macro level, which results in its largest specific surface area and pore volume. This structure is beneficial to photocatalytic reactions, because mesoporous channels can provide the accesses for charges to transport and shorten the paths from bulk to surface, thus suppressing charge recombination.

3.2. Optical and electrochemical properties of g-C₃N₄

The optical absorption of the g-C₃N₄ samples was elucidated by UV–vis diffuse reflection spectra (DRS), as shown in Fig. 7A. All the modified g-C₃N₄ samples exhibit similar optical absorption in comparison to CN, indicating that the intrinsic backbone structure of g-C₃N₄ remains unchanged after the modifications. However, some difference exist in their absorption edges. Thus, the band gap of these g-C₃N₄ samples has been obtained from the (A*hν*)²–*hν* spectra (Fig. 7B), which were transformed from the UV–vis diffuse reflection spectra. The obtained band gap values are listed in Table 2. An evident blue shift in

Table 1
Chemical compositions of the g-C₃N₄ samples.

Samples	Atomic/% (before Ar etching)					Atomic/% (after Ar etching)				
	C	N	O	K	I	C	N	O	K	I
CN	56.78	40.39	2.84	–	–	53.60	44.16	2.24	–	–
MP-CN	56.01	41.18	2.81	–	–	50.75	44.44	2.81	–	–
CN-KI	55.46	38.25	2.66	2.38	0.11	50.28	45.05	1.56	2.09	0.12
MP-CN-KI	57.78	37.15	2.66	2.31	0.10	50.24	44.75	2.82	2.09	0.10

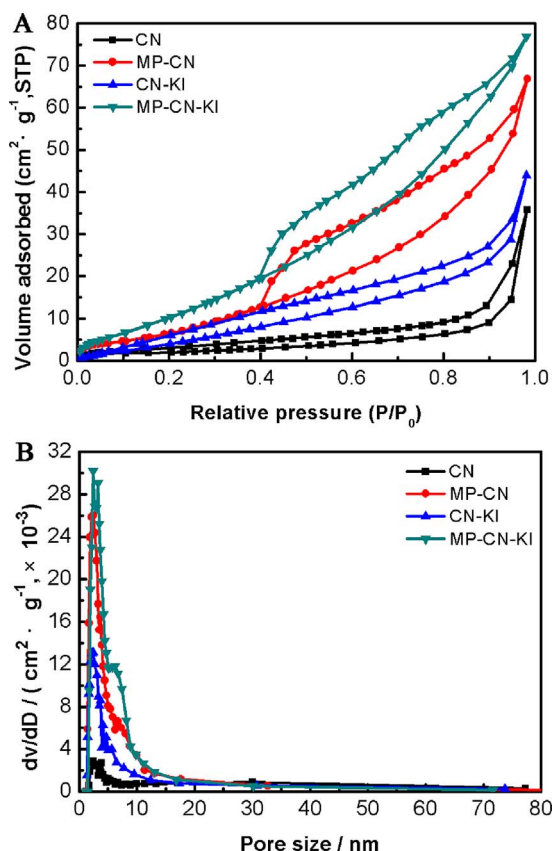


Fig. 4. N₂ adsorption-desorption isotherms (A) and the corresponding pore-size distribution curves (B) of g-C₃N₄ samples.

Table 2
Physicochemical properties and photocatalytic activity of g-C₃N₄ samples for hydrogen evolution with visible light.

Samples	Surface area/ m ² g ^{−1}	Pore volume/ cm ³ g ^{−1}	Band gap/eV	Hydrogen evolution rate/μmol h ^{−1}
CN	8.31	0.055	2.78	8.39
MP-CN	49.09	0.10	2.92	39.73
CN-KI	30.97	0.067	2.67	41.23
MP-CN-KI	71.48	0.12	2.80	80.58

absorption edge is emerged for MP-CN, accordingly the band gap increases from 2.78 eV for CN to 2.92 eV for MP-CN. The increase in band gap can be explicated by a strong quantum confinement effect in the porous samples synthesized in the presence of SBA-15 [60]. It is indicated that the formation of the porous structure narrows the visible light response of CN. Differently, a remarkable red-shift is observed for CN-KI, designating a narrowed band gap of 2.67 eV. According to our previous work [49], the extended visible light response resulted from both the K and I doping, but the I doping played a more effective part in narrowing band gap than the K doping. Compared with MP-CN, MP-CN-

KI exhibits a red shift in absorption edge owing to the doping with K and I, which has a band gap of 2.80 eV, close to that of CN.

Fig. 8A shows the room temperature PL spectra of the g-C₃N₄ samples at the excitation wavelength of 375 nm. A remarkable reduction in the emission peak intensity is distinguished for the modified g-C₃N₄ samples as compared to that of pristine CN, suggesting that both the formation of the porous structure and the doping with KI greatly reduce the recombination of photo-generated charge carriers. For MP-CN, the reduction comes from the existence of ordered mesoporous channels shortening charge transport path. As for CN-KI, the decrease results from the K and I co-doping due to the enhancement in conductivity. Consequently, MP-CN-KI exhibits the lowest emission peak, which is attributed to the synergistic effect between the morphology modification and the K-I co-doping. The enlarged view from 425 to 550 nm for the three samples (the insert in Fig. 8A) displays the differences in PL spectra for MP-CN, CN-KI and MP-CN-KI intuitively. The emission peak is blue shifted for MP-CN and red shifted for CN-KI, while neither a blue shift nor a red shift is observed for MP-CN-KI. It suggests that the formation of the mesoporous structure narrows the visible light absorption range of g-C₃N₄, whereas the co-doping with K and I extends the visible light absorption. As a result, the combination of the mesoporous structure and the doping with KI makes MP-CN-KI exhibit the similar visible light absorption to that of CN. The results from the PL spectra are in accordance with the DRS analyses.

Furthermore, the lifetimes of charge carriers for the g-C₃N₄ samples were further investigated by the time-resolved fluorescence spectra, as shown in Fig. 8B. And the fitting parameters of the radiative lifetimes and their percentages are listed in Table 3. The mean life time for CN is 2.13 ns, in which τ_1 is 1.25 ns with a percentage of 68.62%, and τ_2 is 4.05 ns, accounting for 31.38%. For all the modified CN samples, τ_1 and τ_2 along with their percentages are 1.74 ns, 51.72% and 7.25 ns, 48.28% for MP-CN, 2.36 ns, 45.86% and 7.51 ns, 54.14% for CN-KI, and 2.43 ns, 42.48% and 8.27 ns, 57.52% for MP-CN-KI. These results suggest an increase in τ_1 and a reduction in its percentage along with the increases in τ_2 and its percentage. Consequently, the mean life time is increased to 4.40 ns for MP-CN, 5.14 ns for CN-KI, and 5.79 ns for MP-CN-KI. It is revealed that all the modified CN samples exhibit longer life time than CN, and the co-doping with K and I plays a more effective role in increasing the life time as compared with the formation of the mesoporous structure. And the longest life time is found for MP-CN-KI, implying the existence of a synergistic effect between the formation of the mesoporous structure and the co-doping with K and I.

Photoelectrochemical measurements were employed to investigate the charge transport property of the g-C₃N₄ samples, as shown in Fig. 9. A significant decrease in the semicircular Nyquist plots (Fig. 9A), is observed for the modified g-C₃N₄ samples as compared with pristine CN, demonstrating that the modifications indeed improve the electronic conductivity of the polymer matrix and thus promote the charge separation. It is obvious that MP-CN-KI demonstrates the highest conductivity, which can be explained as follows. On one hand, the ordered mesoporous structure exhibits the reduced resistance for electron transport, thus leading to more effective separation of charges. On the other hand, the doping with KI can effectively promote the electronic conductivity of the polymer matrix to accelerate the charge separation. These results conform to the ones from the PL spectra.

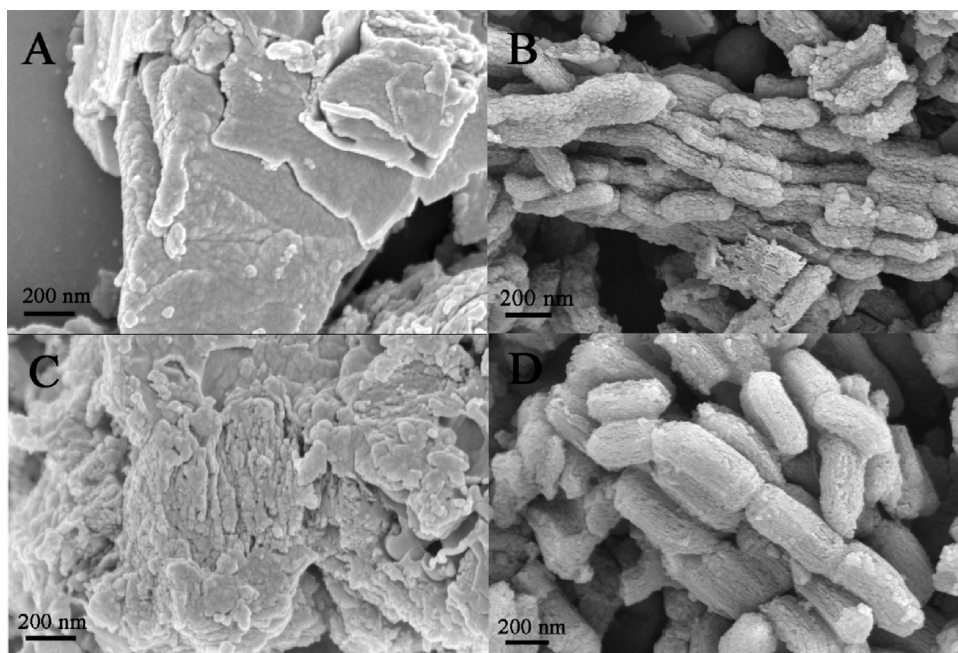


Fig. 5. SEM images of $g\text{-C}_3\text{N}_4$ samples: CN (A), MP-CN (B), CN-KI (C) and MP-CN-KI (D).

The generation and separation of charges on the $g\text{-C}_3\text{N}_4$ electrodes were investigated by analyzing the photocurrent response of the electrodes under visible light irradiation. As shown in Fig. 9B, the photocurrent of the $g\text{-C}_3\text{N}_4$ samples is enhanced after the modifications, indicating the promotion of charge generation and separation. In addition, the photocurrent density of these electrodes is steady and producible during four times' intermittent on/off irradiation cycles, reflecting the good stability of all these samples. Interestingly, the current density of MP-CN-KI leaps to the highest value among all these samples, which is almost 10.5 times that of pristine CN. And the current density of MP-CN-KI is nearly equal to the sum of those of MP-CN and CN-KI, whose current densities are about 5.3 and 5.8 times as that of pristine CN, respectively. The highest current density achieved by MP-CN-KI verifies the synergistic effect between the formation of the mesoporous structure and the co-doping with K and I.

3.3. Photocatalytic activity of $g\text{-C}_3\text{N}_4$

Photocatalytic hydrogen evolution performance of the as-prepared $g\text{-C}_3\text{N}_4$ samples was evaluated under visible light irradiation ($\lambda > 420\text{ nm}$), as shown in Fig. 10A. Obviously, MP-CN and CN-KI both possess the hydrogen evolution rates (HER) of 39.73 and 41.23 $\mu\text{mol/h}$, which are 3.7 and 3.9 times higher than that for CN (8.3 $\mu\text{mol/h}$), respectively. Significantly, the highest hydrogen evolution rate of 80.58 $\mu\text{mol/h}$ is achieved by MP-CN-KI, which is 9.7 times as high as that for CN. Interestingly, the HER for MP-CN-KI is approximately equal to the sum of those for MP-CN and CN-KI, in coincidence with the results of photocurrent density. In addition, the comparison of the DRS spectra and the wavelength dependence of hydrogen evolution plots is further conducted in Fig. S5, the value of hydrogen generation almost keep variation along with the optical

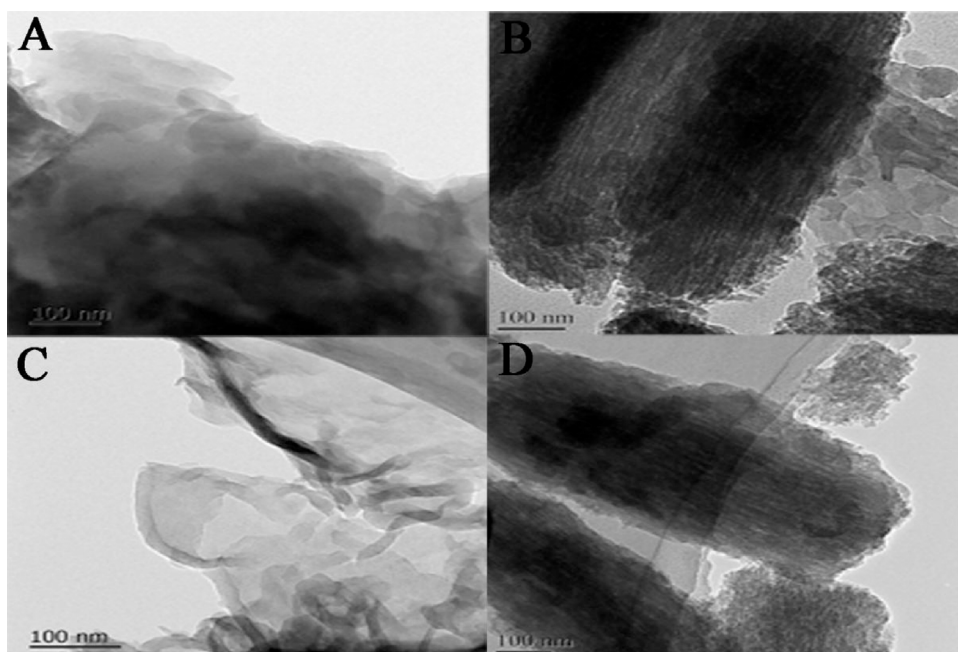


Fig. 6. TEM images of $g\text{-C}_3\text{N}_4$ samples: CN (A), MP-CN (B), CN-KI (C) and MP-CN-KI (D).

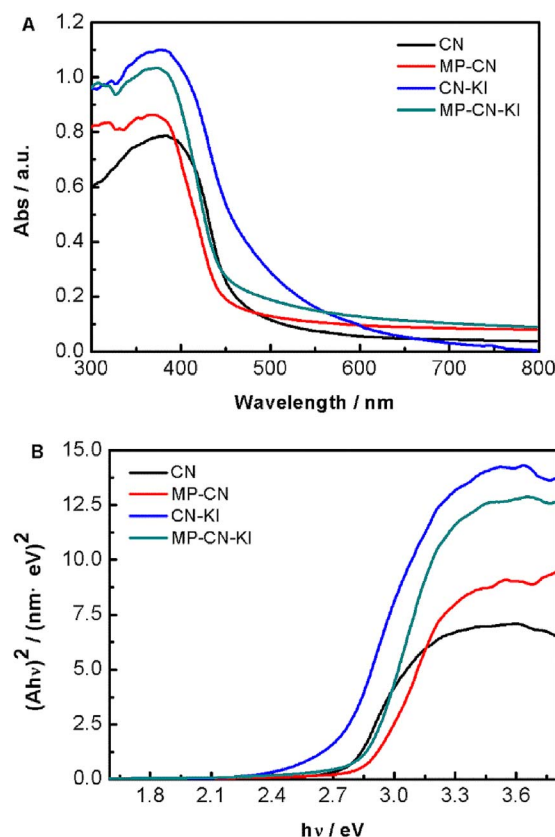


Fig. 7. UV-vis diffuse reflection spectra (A) and the plot of $(\alpha h\nu)^{1/2}$ versus the energy of light ($h\nu$) (B) of g-C₃N₄ samples.

absorption region. And there is still trace hydrogen signal can be investigated when the irradiation wavelength extended to 550 nm which equipped with the band-pass filters, presenting the good optical response property. The increase in photocatalytic hydrogen evolution for MP-CN-KI is ascribed to the synergistic effect between the formation of the mesoporous structure and the co-doping with K and I. Ordered mesoporous channels formed with the aid of SBA-15 provide a readily pore-wall access which is beneficial for the charges to transport from the inward to the surface to shorten the transport paths of excited charges and also the reactant molecule is easy to diffuse into the exposed edges. By this way, more photo-induced charges reach the surface to take part in the catalytic reaction which could dramatically accelerate the photocatalytic reaction in kinetics. In addition, the much larger surface area of MP-CN-KI provides more surface active sites, catalytic sites, and channels for the hydrogen evolution reaction. At the same time, the K and I co-doping improves the electronic property, reduces the charge recombination and enhance the charge carriers lifetimes as well as maintains optical absorption in spite of the quantum confinement effect induced by the mesoporous structure. Consequently, the photocatalytic activity of MP-CN-KI is boosted on account of enlarged surface area and reduced carrier recombination, stemming from the synergistic effect between the formation of the mesoporous structure and the K and I co-doping. It has been noticed that the HER of these g-C₃N₄ samples is in good agreement with the results from PL spectra and photocurrent response, revealing that the determining factor for the photocatalytic activity of g-C₃N₄ is the charge transport and carrier recombination.

What's more, in order to confirm this conclusion, we have prepared another two MP-CN-KI photocatalysts with the additive SBA to be 0.5 and 1.5 g, while the additive SBA of MP-CN-KI in the manuscript is 1 g, and carried out BET, PL and hydrogen evolution experiments. It can be seen from Fig. S1 in the supporting information that the HER of these MP-CN-KI samples is in accordance with the results of PL intensity.

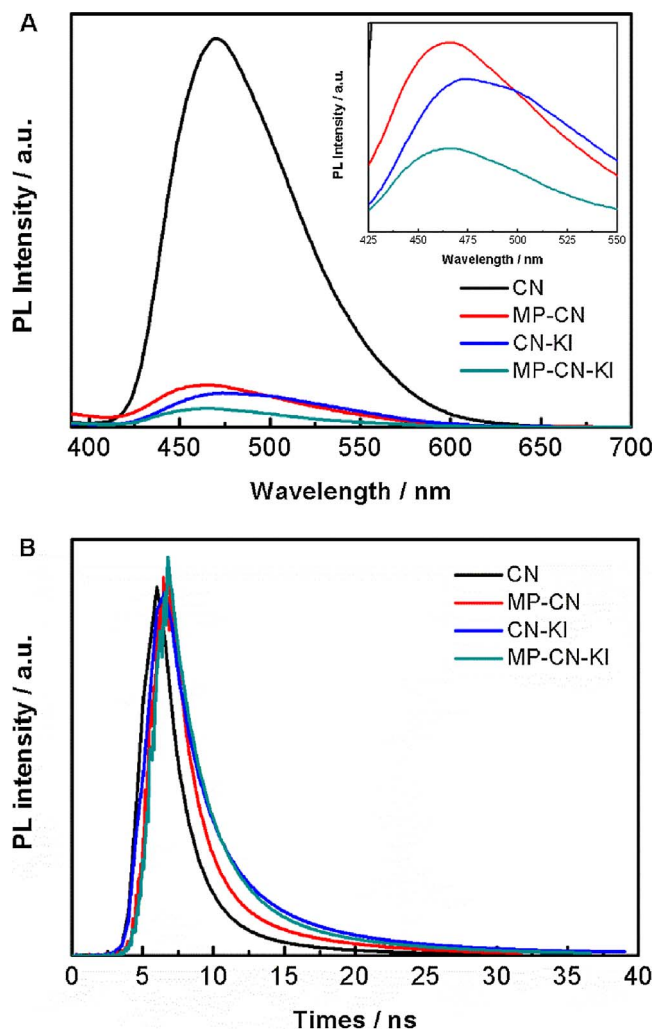


Fig. 8. Photoluminescence spectra (A) and time-resolved fluorescence spectra (B) of g-C₃N₄ samples.

Table 3

The fluorescence decay lifetimes and their percentages of photo-introduced carriers for the g-C₃N₄ samples.

Samples	τ_1 /ns	Rel./%	τ_2 /ns	Rel./%	τ /ns
CN	1.25	68.62	4.05	31.38	2.13
MP-CN	1.74	51.72	7.25	48.28	4.40
CN-KI	2.36	45.86	7.51	54.14	5.14
MP-CN-KI	2.43	42.48	8.27	57.52	5.79

However, the BET results shows that surface areas of MP-CN-KI-0.5, MP-CN-KI-1.0 and MP-CN-KI-1.5 are 56.58, 71.48 and 119.01 m²/g, deviating from the results of HER. These further confirm that the determining factor for the photocatalytic activity of MP-CN-KI is the carrier recombination. Moreover, in order to evaluate the stability and reusability of the MP-CN-KI photocatalyst, the hydrogen production catalyzed by MP-CN-KI was carried out under visible light cycled for five times. As shown in Fig. 10B, no obvious deactivation is observed on the photocatalytic activity of MP-CN-KI after the five consecutive cycle's reactions, indicating that MP-CN-KI has good stability under visible light irradiation. Furthermore, the high resolution XPS C 1s, N 1s, K 2p and I 3d spectras of the comparison between MP-CN-KI-fresh and MP-CN-KI-used are shown in Fig. S4, these can be found the XPS peaks of C 1s and N 1s spectras over the related two sample almost keep the same binding energy, indicating the surface compositions are

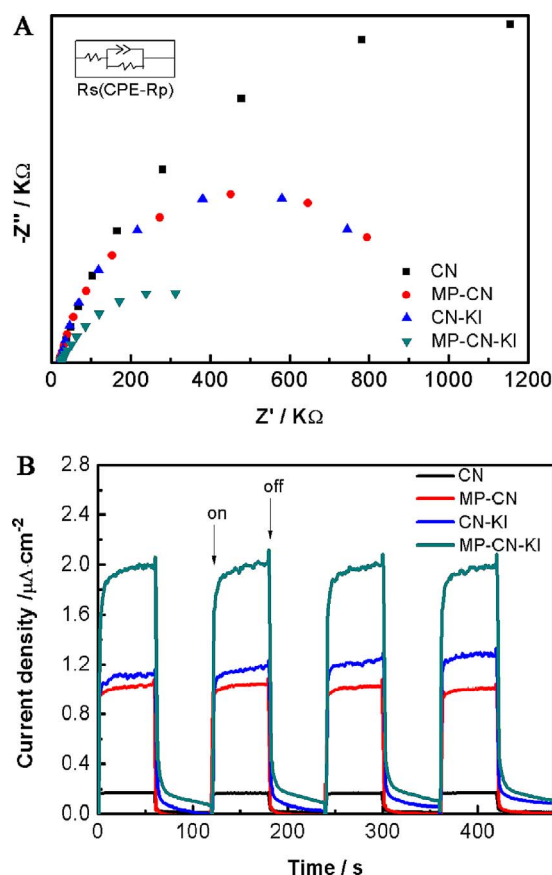


Fig. 9. Electrochemical impedance spectroscopy plots in the dark (A) and periodic on/off photocurrent response under visible light irradiation (B) of g-C₃N₄ samples.

not changed after reaction. And also, from Fig. S4C and Fig. S4D, the typical K 2p and I 3d peaks are observed after reaction, which are in accord with the fresh sample, demonstrating the stability of the surface composition and chemical valence.

4. Conclusions

In summary, the K and I co-doped mesoporous g-C₃N₄ photocatalyst has been successfully prepared by the thermal polymerization using dicyandiamide and potassium iodine as the precursor and dopant, along with SBA-15 as a hard template. The XRD patterns, SEM and TEM images along with the adsorption-desorption isotherms verify the mesoporous structure of the K and I co-doped mesoporous g-C₃N₄ photocatalyst, and the XPS analyses confirm the doping with K and I in it. For the K and I co-doped mesoporous g-C₃N₄ photocatalyst, the blue shift induced by the mesoporous structure is compensated for by the red shift originated from the K and I codoping. The K and I co-doped mesoporous g-C₃N₄ photocatalyst exhibits the longest life time of carriers along with the highest electric conductivity and photocurrent density, which suggest the existence of a synergistic effect between the formation of the mesoporous structure and the co-doping with K and I. The synergistic effect make the K and I co-doped mesoporous g-C₃N₄ photocatalyst achieve the highest hydrogen evolution rate of 80.58 $\mu mol/h$. This paper highlights the importance in the integration of different modification strategies for further increasing the photocatalytic activity of g-C₃N₄-based photocatalysts.

Conflict of interest

The authors declare no competing financial interest.

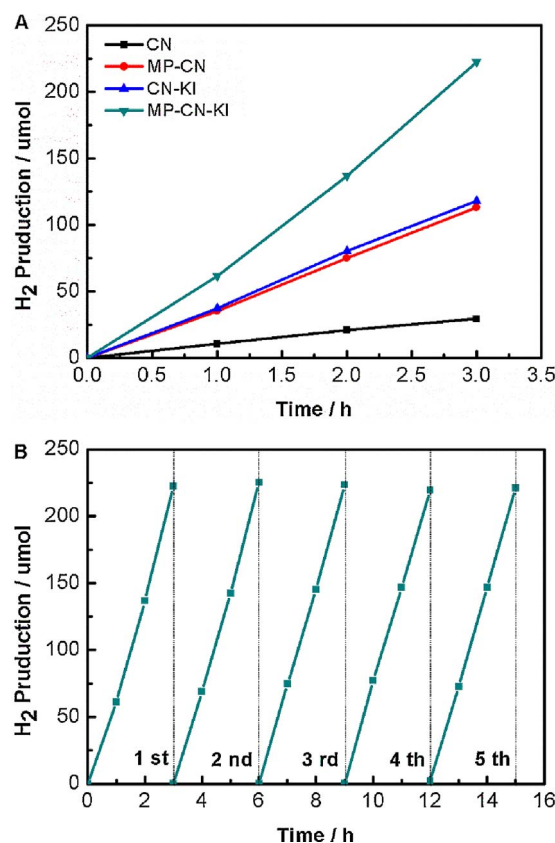


Fig. 10. (A) Photocatalytic H₂ evolution over g-C₃N₄ samples under visible light irradiation and (B) cycle runs of H₂ evolution for the MP-CN-KI photocatalyst.

Author contributions

The manuscript was written through contributions of all authors. All authors have given approval to the final version of the manuscript.

Acknowledgment

This work was supported by the National Natural Science Foundation of China (No. 21276088 and 60976053).

Appendix A. Supplementary data

Supplementary data associated with this article can be found, in the online version, at <http://dx.doi.org/10.1016/j.apcatb.2017.08.075>.

References

- [1] O.K. Dalrymple, E. Stefanakos, M.A. Trotz, D.Y. Goswami, A review of the mechanisms and modeling of photocatalytic disinfection, *Appl. Catal. B: Environ.* 98 (2010) 27–38.
- [2] X. Wang, K. Maeda, A. Thomas, K. Takanabe, G. Xin, J.M. Carlsson, K. Domen, M. Antonietti, A metal-free polymeric photocatalyst for hydrogen production from water under visible light, *Nat. Mater.* 8 (2009) 76–80.
- [3] K. Zhang, L. Guo, Metal sulphide semiconductors for photocatalytic hydrogen production, *Catal. Sci. Technol.* 3 (2013) 1672.
- [4] R.A. He, S. Cao, P. Zhou, J. Yu, Recent advances in visible light Bi-based photocatalysts, *Chin. J. Catal.* 35 (2014) 989–1007.
- [5] X. Li, J.G. Yu, M. Jaroniec, Hierarchical photocatalysts, *Chem. Soc. Rev.* 45 (2016) 2603–2636.
- [6] Y. Zheng, J. Liu, J. Liang, M. Jaroniec, S.Z. Qiao, Graphitic carbon nitride materials: controllable synthesis and applications in fuel cells and photocatalysis, *Energy Environ. Sci.* 5 (2012) 6717.
- [7] Q. Liu, Y. Guo, Z. Chen, Z. Zhang, X. Fang, Constructing a novel ternary Fe(III)/graphene/g-C₃N₄ composite photocatalyst with enhanced visible-light driven photocatalytic activity via interfacial charge transfer effect, *Appl. Catal. B-Environ.* 183 (2016) 231–241.
- [8] G. Zhang, Z.-A. Lan, L. Lin, S. Lin, X. Wang, Overall water splitting by Pt/g-

- C3N4 photocatalysts without using sacrificial agents, *Chem. Sci.* 7 (2016) 3062–3066.
- [9] X. Rong, F. Qiu, H. Zhao, J. Yan, X. Zhu, D. Yang, Fabrication of single-layer graphitic carbon nitride and coupled systems for the photocatalytic degradation of dyes under visible-light irradiation, *Eur. J. Inorg. Chem.* 2015 (2015) 1359–1367.
 - [10] S. Hu, L. Ma, J. You, F. Li, Z. Fan, G. Lu, D. Liu, J. Gui, Enhanced visible light photocatalytic performance of g-C3N4 photocatalysts co-doped with iron and phosphorus, *Appl. Surf. Sci.* 311 (2014) 164–171.
 - [11] S. Cao, J. Low, J. Yu, M. Jaroniec, Polymeric photocatalysts based on graphitic carbon nitride, *Adv. Mater.* 27 (2015) 2150–2176.
 - [12] J. Zhang, B. Wang, X. Wang, Carbon nitride polymeric semiconductor for photocatalysis, *Prog. Chem.* 26 (2014) 19–29.
 - [13] Q. Liu, T.X. Chen, Y.R. Guo, Z.G. Zhang, X.M. Fang, Ultrathin g-C3N4 nanosheets coupled with carbon nanodots as 2D/0D composites for efficient photocatalytic H2 evolution, *Appl. Catal. B-Environ.* 193 (2016) 248–258.
 - [14] Q. Liu, T. Chen, Y. Guo, Z. Zhang, X. Fang, Grafting Fe(III) species on carbon nanodots/Fe-doped g-C3N4 via interfacial charge transfer effect for highly improved photocatalytic performance, *Appl. Catal. B: Environ.* 205 (2017) 173–181.
 - [15] P. Yang, H. Ou, Y. Fang, X. Wang, A facile steam reforming strategy to delaminate layered carbon nitride semiconductors for photoredox catalysis, *Angew. Chem.* 56 (2017) 3992–3996.
 - [16] Y. Zheng, L. Lin, B. Wang, X. Wang, Graphitic carbon nitride polymers toward sustainable photoredox catalysis, *Angew. Chem.* 54 (2015) 12868–12884.
 - [17] Y. Shang, X. Chen, W. Liu, P. Tan, H. Chen, L. Wu, C. Ma, X. Xiong, J. Pan, Photocorrosion inhibition and high-efficiency photoactivity of porous g-C3N4/Ag2CrO4 composites by simple microemulsion-assisted co-precipitation method, *Appl. Catal. B: Environ.* 204 (2017) 78–88.
 - [18] M. Aleksandrak, W. Kukulka, E. Mijowska, Graphitic carbon nitride/graphene oxide/reduced graphene oxide nanocomposites for photoluminescence and photocatalysis, *Appl. Surf. Sci.* 398 (2017) 56–62.
 - [19] Z. Mao, J. Chen, Y. Yang, D. Wang, L. Bie, B.D. Fahlman, Novel g-C3N4/CoO nanocomposites with significantly enhanced visible-light photocatalytic activity for H2 evolution, *ACS Appl. Mater. Interfaces* (2017).
 - [20] C. Cheng, J. Shi, Y. Hu, L. Guo, WO3/g-C3N4 composites: one-pot preparation and enhanced photocatalytic H2 production under visible-light irradiation, *Nanotechnology* 28 (2017) 164002.
 - [21] F. Dong, Z. Zhao, T. Xiong, Z. Ni, W. Zhang, Y. Sun, W.K. Ho, In situ construction of g-C3N4/g-C3N4 metal-free heterojunction for enhanced visible-light photocatalysis, *ACS Appl. Mater. Interfaces* 5 (2013) 11392–11401.
 - [22] Z. Chen, P. Sun, B. Fan, Q. Liu, Z. Zhang, X. Fang, Textural and electronic structure engineering of carbon nitride via doping with π -deficient aromatic pyridine ring for improving photocatalytic activity, *Appl. Catal. B: Environ.* 170–171 (2015) 10–16.
 - [23] Z.-A. Lan, G. Zhang, X. Wang, A facile synthesis of Br-modified g-C3N4 semiconductors for photoredox water splitting, *Appl. Catal. B: Environ.* 192 (2016) 116–125.
 - [24] J. Qin, S. Wang, H. Ren, Y. Hou, X. Wang, Photocatalytic reduction of CO2 by graphitic carbon nitride polymers derived from urea and barbituric acid, *Appl. Catal. B: Environ.* 179 (2015) 1–8.
 - [25] X. Bai, L. Wang, R. Zong, Y. Zhu, Photocatalytic activity enhanced via g-C3N4/Nanoplates to nanorods, *J. Phys. Chem. C* 117 (2013) 9952–9961.
 - [26] J. Tian, Q. Liu, A.M. Asiri, X. Sun, Y. He, Ultrathin graphitic C3N4 nanofibers: hydrolysis-driven top-down rapid synthesis and application as a novel fluorosensor for rapid, sensitive, and selective detection of Fe3+, *Sens. Actuators B: Chem.* 216 (2015) 453–460.
 - [27] B. Lin, C. Xue, X. Yan, G. Yang, G. Yang, B. Yang, Facile fabrication of novel SiO2/g-C3N4 core-shell nanosphere photocatalysts with enhanced visible light activity, *Appl. Surf. Sci.* 357 (2015) 346–355.
 - [28] Z. Tong, D. Yang, Z. Li, Y. Nan, F. Ding, Y. Shen, Z. Jiang, Thylakoid-inspired multishell g-C3N4 nanocapsules with enhanced visible-light harvesting and electron transfer properties for high-efficiency photocatalysis, *ACS Nano* 11 (2017) 1103–1112.
 - [29] D. Zheng, X.N. Cao, X. Wang, Precise formation of a hollow carbon nitride structure with a janus surface to promote water splitting by photoredox catalysis, *Angew. Chem.* 55 (2016) 11512–11516.
 - [30] H. Ou, L. Lin, Y. Zheng, P. Yang, Y. Fang, X. Wang, Tri-s-triazine-based crystalline carbon nitride nanosheets for an improved hydrogen evolution, *Adv. Mater.* 29 (2017).
 - [31] W. Shan, Y. Hu, Z. Bai, M. Zheng, C. Wei, In situ preparation of g-C3N4/bismuth-based oxide nanocomposites with enhanced photocatalytic activity, *Appl. Catal. B: Environ.* 188 (2016) 1–12.
 - [32] H. Xu, J. Yan, Y. Xu, Y. Song, H. Li, J. Xia, C. Huang, H. Wan, Novel visible-light-driven AgX/graphite-like C3N4 (X = Br, I) hybrid materials with synergistic photocatalytic activity, *Appl. Catal. B: Environ.* 129 (2013) 182–193.
 - [33] Y. Liu, J. Wang, P. Yang, Photochemical reactions of g-C3N4-based heterostructured composites in Rhodamine B degradation under visible light, *RSC Adv.* 6 (2016) 34334–34341.
 - [34] D. Zheng, G. Zhang, X. Wang, Integrating CdS quantum dots on hollow graphitic carbon nitride nanospheres for hydrogen evolution photocatalysis, *Appl. Catal. B: Environ.* 179 (2015) 479–488.
 - [35] Y. Hou, Y. Zhu, Y. Xu, X. Wang, Photocatalytic hydrogen production over carbon nitride loaded with WS2 as cocatalyst under visible light, *Appl. Catal. B: Environ.* 156–157 (2014) 122–127.
 - [36] Y.D. Yin, R.M. Rioux, C.K. Erdonmez, S. Hughes, G.A. Somorjai, A.P. Alivisatos, Formation of hollow nanocrystals through the nanoscale Kirkendall Effect, *Science* 304 (2004) 711–714.
 - [37] G. Dong, L. Zhang, Porous structure dependent photoreactivity of graphitic carbon nitride under visible light, *J. Mater. Chem.* 22 (2012) 1160–1166.
 - [38] Z.-F. Huang, J. Song, L. Pan, Z. Wang, X. Zhang, J.-J. Zou, W. Mi, X. Zhang, L. Wang, Carbon nitride with simultaneous porous network and O-doping for efficient solar-energy-driven hydrogen evolution, *Nano Energy* 12 (2015) 646–656.
 - [39] M. Wu, J.M. Yan, X.N. Tang, M. Zhao, Q. Jiang, Synthesis of potassium-modified graphitic carbon nitride with high photocatalytic activity for hydrogen evolution, *ChemSusChem* 7 (2014) 2654–2658.
 - [40] S. Hu, F. Li, Z. Fan, F. Wang, Y. Zhao, Z. Lv, Band gap-tunable potassium doped graphitic carbon nitride with enhanced mineralization ability, *Dalton Trans.* 44 (2015) 1084–1092.
 - [41] B. Yue, Q. Li, H. Iwai, T. Kako, J. Ye, Hydrogen production using zinc-doped carbon nitride catalyst irradiated with visible light, *Sci. Technol. Adv. Mater.* 12 (2011) 034401.
 - [42] J. Chen, Z. Hong, Y. Chen, B. Lin, B. Gao, One-step synthesis of sulfur-doped and nitrogen-deficient g-C3N4 photocatalyst for enhanced hydrogen evolution under visible light, *Mater. Lett.* 145 (2015) 129–132.
 - [43] G. Zhang, M. Zhang, X. Ye, X. Qiu, S. Lin, X. Wang, Iodine modified carbon nitride semiconductors as visible light photocatalysts for hydrogen evolution, *Adv. Mater.* 26 (2014) 805–809.
 - [44] J. Hong, X. Xia, Y. Wang, R. Xu, Mesoporous carbon nitride with in situ sulfur doping for enhanced photocatalytic hydrogen evolution from water under visible light, *J. Mater. Chem.* 22 (2012) 15006–15012.
 - [45] L.J. Fang, X.L. Wang, J.J. Zhao, Y.H. Li, Y.L. Wang, X.L. Du, Z.F. He, H.D. Zeng, H.G. Yang, One-step fabrication of porous oxygen-doped g-C3N4 with feeble nitrogen vacancies for enhanced photocatalytic performance, *Chem. Commun.* 52 (2016) 14408–14411.
 - [46] N. Bao, X. Hu, Q. Zhang, X. Miao, X. Jie, S. Zhou, Synthesis of porous carbon-doped g-C3N4 nanosheets with enhanced visible-light photocatalytic activity, *Appl. Surf. Sci.* 403 (2017) 682–690.
 - [47] S. Le, T. Jiang, Q. Zhao, X. Liu, Y. Li, B. Fang, M. Gong, Cu-doped mesoporous graphitic carbon nitride for enhanced visible-light driven photocatalysis, *RSC Adv.* 6 (2016) 38811–38819.
 - [48] Y.P. Zhu, T.Z. Ren, Z.Y. Yuan, Mesoporous phosphorus-doped g-C3N4 nanostructured flowers with superior photocatalytic hydrogen evolution performance, *ACS Appl. Mater. Interfaces* 7 (2015) 16850–16856.
 - [49] Y. Guo, T. Chen, Q. Liu, Z. Zhang, X. Fang, Insight into the enhanced photocatalytic activity of potassium and iodine codoped graphitic carbon nitride photocatalysts, *J. Phys. Chem. C* 120 (2016) 25328–25337.
 - [50] J. Zhang, G. Zhang, X. Chen, S. Lin, L. Mohlmann, G. Dolega, G. Lipner, M. Antonietti, S. Blechert, X. Wang, Co-monomer control of carbon nitride semiconductors to optimize hydrogen evolution with visible light, *Angew. Chem.* 51 (2012) 3183–3187.
 - [51] J. Zhang, X. Chen, K. Takanabe, K. Maeda, K. Domen, J.D. Epping, X. Fu, M. Antonietti, X. Wang, Synthesis of a carbon nitride structure for visible-light catalysis by copolymerization, *Angew. Chem.* 49 (2010) 441–444.
 - [52] L.B. Sun, J. Yang, J.H. Kou, F.N. Gu, Y. Chun, Y. Wang, J.H. Zhu, Z.G. Zou, One-pot synthesis of potassium-functionalized mesoporous gamma-alumina: a solid superbase, *Angew. Chem.* 47 (2008) 3418–3421.
 - [53] C. Yanjuan, Z. Jinshui, Z. Guigang, H. Jianhui, L. Ping, M. Antonietti, W. Xinchun, Synthesis of bulk and nanoporous carbon nitride polymers from ammonium thiocyanate for photocatalytic hydrogen evolution, *J. Mater. Chem.* 21 (2011) 13032–13039.
 - [54] C. Bi, Y. Zhao, L. Shen, K. Zhang, X. He, L. Chen, Y. Zhang, Click synthesis of hydrophilic maltose-Functionalized iron oxide magnetic nanoparticles based on dopamine anchors for highly selective enrichment of glycopeptides, *ACS Appl. Mater. Interfaces* 7 (2015) 24670–24678.
 - [55] H. Gao, S. Yan, J. Wang, Y.A. Huang, P. Wang, Z. Li, Z. Zou, Towards efficient solar hydrogen production by intercalated carbon nitride photocatalyst, *Phys. Chem. Chem. Phys.* 15 (2013) 18077–18084.
 - [56] Y. Bu, Z. Chen, Role of polyaniline on the photocatalytic degradation and stability performance of the polyaniline/silver/silver phosphate composite under visible light, *ACS Appl. Mater. Interfaces* 6 (2014) 17589–17598.
 - [57] J. Zhang, F. Guo, X. Wang, An optimized and general synthetic strategy for fabrication of polymeric carbon nitride nanoarchitectures, *Adv. Funct. Mater.* 23 (2013) 3008–3014.
 - [58] M. Zhang, X. Bai, D. Liu, J. Wang, Y. Zhu, Enhanced catalytic activity of potassium-doped graphitic carbon nitride induced by lower valence position, *Appl. Catal. B: Environ.* 164 (2015) 77–81.
 - [59] O.Y. Khyzhun, P.M. Fochuk, I.V. Kityk, M. Piasecki, S.I. Levkovets, A.O. Fedorchuk, O.V. Parasyuk, Single crystal growth and electronic structure of TIPbI3, *Mater. Chem. Phys.* 172 (2016) 165–172.
 - [60] J. Liu, J. Yan, H. Ji, Y. Xu, L. Huang, Y. Li, Y. Song, Q. Zhang, H. Xu, H. Li, Controlled synthesis of ordered mesoporous g-C3N4 with a confined space effect on its photocatalytic activity, *Mater. Sci. Semicond. Process.* 46 (2016) 59–68.
 - [61] B. Tian, S. Liu, S. Wu, W. Lu, D. Wang, L. Jin, B. Hu, K. Li, Z. Wang, Z. Quan, pH-responsive poly (acrylic acid)-gated mesoporous silica and its application in oral colon targeted drug delivery for doxorubicin, *Colloids Surf. B Biointerfaces* 154 (2017) 287–296.